Laboratory Measurements of Light Scattering by Single Levitated Ice Crystals

NEIL J. BACON

Physics Program, University of Washington, Seattle, Washington

BRIAN D. SWANSON

Geophysics Program, University of Washington, Seattle, Washington

(Manuscript received 26 April 1999, in final form 16 August 1999)

ABSTRACT

The authors have measured the differential light-scattering cross sections and phase functions of single vapor-grown hexagonal ice particles levitated in an electrodynamic balance. The ice particles, grown at temperatures $-5^\circ > T > -10$°C, were typically ≈50 μm in diameter and tended to orient with the c axis either nearly vertical (parallel to the scattering plane normal) or horizontal (in the scattering plane). Helium–neon laser light scattered by a levitated crystal was collected in the angular ranges 20°–65° and 115°–160° with a 1024-element linear photodiode array with an angular resolution of about 0.05°. The particle size and orientation were measured a few seconds before and after the scattering measurements with top- and side-view video telemicroscopes. Three basic features are found in the scattering from vertically aligned crystals: (i) a strong ''halo'' peak between about 21° and 35°, (ii) a secondary peak with ripple structure between about 30° and 70°, and (iii) a weaker peak in the backscatter between 115° and 160°. The ripple structure is interpreted in terms of two-beam interference and is shown to provide a sensitive measure of crystal dimensions. The experimentally measured peak positions are compared with a simple model, and the authors discuss the effects of surface roughness, crystal imperfections, and tilted orientations on the measured scattering cross sections.

1. Introduction

The uncertainty in the angular distribution of light scattered from small ice particles is one major source of error in radiative transfer models (Stephens et al. 1990; Vogelmann and Ackerman 1995). The observation of various halo phenomena and simple geometrical arguments give clear evidence to the fact that scattering from a collection of randomly oriented nonspherical particles is not equivalent to a suitably chosen collection of spheres (see, e.g., Greenler 1980). Of particular importance to climate modelers is the scattering phase function $P(\Omega', \Omega)$, which represents the distribution of scattered energy as a function of incoming and outgoing directions Ω' and Ω. The most important information contained in $P(\Omega', \Omega)$ is the degree to which particles scatter light in forward directions. This can be expressed in terms of the asymmetry factor g (Bohren and Huffman 1983; Takano and Liou 1989), to which climate models are highly sensitive (Stephens et al. 1990). The magnitude of g for various particle types remains in question; Takano and Liou (1989, 1995) find $g > 0.8$, while measurements made during the First International Satellite Cloud Climatology Project (ISCCP) Regional Experiment (FIRE) 1991 (Kinne et al. 1992; Stackhouse and Stephens 1991) were consistent with $g \sim 0.7$. Hess et al. (1998) give g as high as 0.94 for large plates and 0.74 for polycrystals.

Until very recently, cloud and climate modelers have estimated the scattering by atmospheric ice particles using known analytic expressions for the phase functions of spheres or cylinders (see, e.g., Bohren and Huffman 1983). T-matrix methods have also been applied to calculate the scattering from axisymmetric particles (Mishchenko et al. 1996). Finite-difference time domain methods (Taflove 1995; Yang and Liou 1995; Yang and Liou 1996) and discrete-dipole methods (see, e.g., Draine and Flatau 1994) have recently been developed to calculate scattering by nonspherical particles, although these methods are applicable only for particles with size parameters $x < 20$ ($x = 2\pi r/\lambda$, where r is a suitably defined crystal radius). Of particular interest has been the scattering by randomly oriented hexagonal columns and plates, which has been calculated primarily with ray-tracing techniques (Cai and Liou 1982; Takano and Jayaweera 1985; Takano and Liou 1989) and ray by ray integration methods (Yang and Liou 1996, 1997). Ray

Corresponding author address: Brian Swanson, Geophysics Program, University of Washington, Box 351650, Seattle, WA 98195-1650.
E-mail: brian@geophys.washington.edu

© 2000 American Meteorological Society

tracing has also been used to model scattering from more complex ice crystal shapes (Macke 1993; Macke et al. 1996; Hess et al. 1998). Traditional ray-tracing schemes omit aspects of scattering associated with the wave nature of light such as interference and beam spreading (meaning the phenomenon whereby a scattered beam diverges from the path defined by strict geometrical optics and achieves finite angular width), and recent models that include such effects (Muinonen 1989; Yang and Liou 1997; Rother et al. 1997) have not been tested experimentally. To date, ray-tracing models have not been tested against measured scattering from ice particles with well-known shapes and orientations, and only a few rudimentary comparisons have been made with cloud data or with analog scattering data from macroscopic objects.

Experimental efforts to measure scattering from single well-characterized nonspherical particles have been quite limited. Analog experiments scattering He–Ne laser light from macroscopic hexagonal crystals of sodium fluoride (Barkey et al. 1999) did provide careful control of the crystal orientation and do show reasonable agreement between the measured scattering and geometric ray-tracing calculations. However, the size parameter for these experiments was orders of magnitude larger than that of atmospheric ice crystals. Microwave analog experiments (Gustafson 1996) can reproduce the size parameter, but analog experiments in general cannot realistically tackle the effects of roughness and imperfections of real ice crystals. Pluchino (1986, 1987) measured light scattering by an electrodynamically levitated 100-μm ice crystal with an angular resolution of about 3°. Although these data show the 22° and the 46° halo features, the exact size, shape, and orientation of the crystal was unknown.

Measurements have been made in both tropospheric clouds (see, e.g., Francis 1995; Lawson et al. 1998) and in artificial ice clouds (e.g., Dugin et al. 1971; Dugin and Mirumyantz 1976; Sassen and Liou 1979; Volkovitskii et al. 1980; Rimmer and Saunders 1997; Sasaki et al. 1998). In the latter case, the goal has been to measure predominantly single scattering from a large number of particles over a wide range of angles. To date, comparisons with computer simulations (e.g., Takano and Liou 1994; Rimmer and Saunders 1997; Sasaki et al. 1998) have not been particularly successful, in part because it is difficult to characterize the distribution, sizes, shapes, and orientations over the entire population of the cloud. Measurements of scattering by individual well-oriented ice particles hold out the possibility of a much cleaner test of single-scattering theories.

A large portion of ice crystals occurring in the troposphere have a hexagonal structure (Heymsfield and Knollenberg 1972), although recent field observations of cirrus particles have highlighted the importance of complex and irregular shapes (e.g., Francis 1995). To facilitate comparison with crystal light-scattering models, we set out to grow crystals with the simplest of crystal habits (hexagonal columns and plates) and to measure the differential scattering cross sections for well-characterized orientations. By careful characterization of particle size, shape, and orientation, we can compare our measured scattering with model calculations. In doing this, we attempt to answer the question of whether geometric optics is a reasonable approximation for the scattering from these particles. We report measurements of scattering from hexagonal crystals with the *c* axis both parallel and perpendicular to the scattering plane normal. In this paper we shall concentrate mainly on the former case (e.g., vertically aligned columns) because these orientations are easy to characterize experimentally and produce strong scattering features that we will show to depend in a simple way on the measured orientation. We chose to measure scattering in the range $20° < \theta < 65°$ because this range contains interesting scattering maxima that can be measured against a low background noise level.

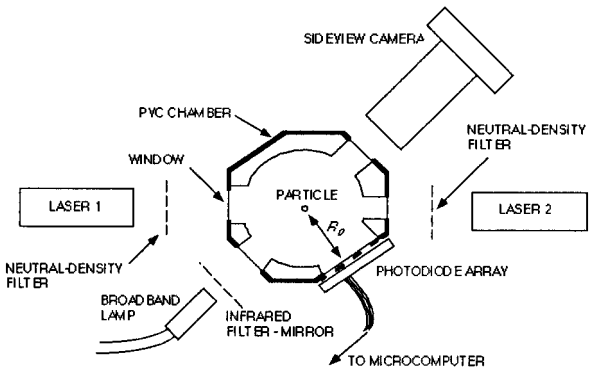

FIG. 1. Schematic top view of the scattering geometry. The orientation corresponds to that seen by the top-view camera (not shown). The photodiode array is 2.75 cm long and contains 1024 elements that detect scattered light in the angular ranges 20°–65° (laser 1) and 115°–160° (laser 2). The distance R_0 from particle to array is 3 cm.

2. Experiment

a. Apparatus and experimental procedure

The apparatus, situated in a cold room, has been described in detail elsewhere (Bacon et al. 1998a,b; Swanson et al. 1999). It consists of an electrodynamic balance (EDB) mounted inside a cylindrical diffusion chamber with glass windows on the chamber top, bottom, and sides for illumination; light-scattering measurements; and optical microscopy. The geometry of the experimental setup is shown in Fig. 1. Single ice particles were levitated and stabilized dynamically at the chamber center (or balance point) by a superposition of DC and AC electric fields. The growth or sublimation rate of a trapped particle was set by a combination of infrared (IR) heating from a broadband light source and the temperature gradient between two temperature-controlled ice surfaces situated at the upper and lower endcaps of the diffusion chamber.

We define the scattering angle θ to be the total deviation angle. The scattered He–Ne laser light intensity was measured with a linear photodiode array of length 2.54 cm consisting of 1024-diode elements that are individually 15 μm across and 250 μm high, subtending a vertical angle of about 0.5° at the particle. The array was positioned to measure forward scattering in the range $20° < \theta < 65°$ in the horizontal (or scattering) plane at a distance of 3 cm (about 10^4 particle diameters) from the particle, effectively in the far field. A second He–Ne laser was positioned diametrically opposite to the first to measure the scattering for $115° < \theta < 160°$ with the same photodiode array. Note that, because the laser used for backscatter measurements was at 180° to the forward-scatter laser, the crystal orientation is different for forward and backscatter measurements. For the data shown in this paper, the laser polarization was vertical ($\hat{z}$), although we also made some measurements with horizontal polarization. To date, we have not observed systematic differences between the two polarization states, but we plan to study the expected differences in future experiments. Calibrated neutral-density filters were used to prevent saturation of the photodiodes. Two video telemicroscopes recorded bright-field stroboscopic side- and top-view images of the particle side by side on VHS for subsequent analysis of particle shape, size, and orientation.

A frost particle was ''flicked'' into the EDB (Bacon et al. 1998a) from the bottom endcap and sublimated to a few micrometer diameter ''seed.'' The seed was then grown over ~1 h, generally to a single hexagonal column or plate with flat facets (see Swanson et al. 1999 for details). For the data shown here, the ice crystals were grown at $-5° > T > -10$°C and at saturation ratios (with respect to ice) between 1.00 and 1.01. We stabilized the particle alignment and maintained faceted crystal habits by setting the EDB to slow growth conditions (less than 0.1 μm min^{-1}). The particles oscillate in the balance with an amplitude of up to 50 μm, but particles bigger than about 20 μm in diameter maintained their orientation despite this oscillation.

During the light-scattering measurement, the diffuse backlighting was turned off and the particle was illuminated with polarized He–Ne laser light, prealigned with the balance point of the chamber, such that the particles were bathed in a beam approximately 10 times their size. We measured scattering intensities in series of 15 scans (scan series) taken in three groups of five about 5 s apart. For a single scan each CCD photodiode accumulates charge (proportional to the scattered light intensity) for a period of about 20 ms. We found that we could measure both forward and backscattering in a single scan series by making the necessary changes (laser shutters, etc.) between scan groups.

We measure the particle orientation from the top- and side-view images taken before and after each scan series, using digitized images grabbed from videotape. The finite shutter speed and small depth of field set the optical resolution at a few microns. During the time (about 30 s) needed to make the scattering measurement, some change in particle orientation occurred. Since the particles were in a state of growth, they tended to fall slightly (but not out of the laser beam), and in doing so rotating by a few degrees. The data we report here consists of over 80 scan series from 7 separate ice crystals, all single columns or plates grown from frost particle seeds, for which the particle orientations measured before and after a scan series matched each other to within a few degrees. Equilateral hexagons were rare (adjacent *a* faces often differed in length by a factor of up to 2), but the crystals were hexagonal in the sense that the internal angle between adjacent *a* faces was 120°. Such asymmetries are common in ice crystals collected in clouds and may have a significant impact on their scattering properties. The growing crystals nearly always developed flat facets over a timescale of a few minutes, during which time we observed the characteristic scattering features develop and sharpen.

b. Calibration

To calibrate the scattering angle θ, we placed a diffraction grating (600 lines mm^{-1}) at the EDB balance point. We were able to do this to within 50 μm by translating the grating until the lines were in focus for the side-view camera, which had been previously focused on a levitated particle. Two diffraction peaks from the He–Ne laser light at 22.3° and 49.4° were used to calibrate the scattering angle for each diode element, consistent with the known geometry. We found that the diode array could be removed and replaced to within 0.5° of the original position and within 0.5 mm of the horizontal plane containing the balance point of the EDB. Overall, we estimate the uncertainty in scattering angle θ to be about 1°.

We found the photodiode array to be spatially uniform to within 5% and linear to within 1% (tested by means of neutral-density filters of known optical depth). We measured the incident intensity I_0 by translating our array across the laser beam, modulated by suitable neutral-density filters, with the maximum intensity taken to be I_0. The spatial profile of the incident laser beam, also measured with the photodiode array, was found to be flat to within 10% over a 300-μm range at the peak intensity. The laser is stable with respect to drift in amplitude to within 6% (manufacturer's specifications). We estimate the point-spread function of the array to be less than 0.1° from our measurements of the diffraction grating signal.

The ratio of the measured intensity I_m to the incident intensity I_0 was used to calculate the differential scattering cross section as follows (see, e.g., Bohren and Huffman 1983):

$$\frac{d\sigma}{d\Omega} = \frac{I_m R_0^2}{I_0 \cos^3\gamma}, \tag{1}$$

where R_0 is the perpendicular distance from the particle to the array (see Fig. 1) and γ is the angle of incidence of the scattered light on the array. The $\cos^3 \gamma$ term arises from the variation of distance from the particle to the array element and obliqueness of incidence. Additional corrections are made to compensate for reflections at the window and the incident intensity I_0 was adjusted for the two different laser intensities and the transmittance of the neutral-density filters. To convert the differential scattering cross section to a phase function one must normalize by the total scattering cross section, a quantity that is difficult to measure. For nonabsorbing large particles (large compared with the wavelength), the total scattering cross section is twice the projected area (Bohren and Huffman 1983), which we are able to measure optically and thereby convert our data to phase functions. Calibration of our optical system, achieved by imaging the diffraction grating, has been described elsewhere (Bacon et al. 1998a). Crystal size measurements taken from the top- and side-view images were estimated to be accurate to within 5%.

c. Characterization of particle orientation and scattering angle

The geometry of light scattering by a nonspherical particle is described by four independent angles. This can be achieved by defining both incoming and outgoing directions relative to crystallographic axes. An alternative description better suited to our experimental setup is to specify the ice crystal orientation in the EDB with respect to the direction of the incident laser beam and fixed scattering plane by the Euler angles χ, α, and β. The fourth angle in the problem is θ, the scattering angle. These angles are defined in Fig. 2, in which the incident beam direction is $\hat{y}$ and the scattering plane is the $\hat{x}$–$\hat{y}$ plane. The angle between $\hat{c}$ (the basal face normal) and $\hat{z}$ (the scattering plane normal) is χ and the orientation of the tilt plane (the $\hat{c}$–$\hat{z}$ plane) with respect to the $\hat{y}$ direction is defined by the angle α. Rotation of the particle about its $\hat{c}$ axis is described by β, the angle (defined modulo 60° for symmetric hexagonal particles) between the $-\hat{y}$ direction and the projection of the prism face normal onto the $\hat{x}$–$\hat{y}$ scattering plane. Experimental characterization of the shape and orientation of an arbitrary crystal presents a considerable challenge. Fortunately, particles were nearly hexagonally symmetric and in our balance tend to align either (i) ''vertically'' ($\hat{c}$ parallel to $\hat{z}$, $\chi \approx 0$), in which case the orientation is defined by β alone, or (ii) ''horizontally'' ($\hat{c}$ perpendicular to $\hat{z}$, $\chi \approx 90°$). For near vertical alignment, the c-axis tilt χ was measured using the side-view image and the angle of incidence β on the relevant a face was measured on top-view images taken before and after the scattering measurement: if these values agreed to within 10°, we used the mean value, otherwise we rejected the data. The uncertainty in β was about 4°, depending on the degree of rotation that took place during the scan series. For horizontal orientations, α was measured using the top-view image. Note that, for an arbitrarily oriented polyhedral particle, the scattering is in general not symmetric about the $\hat{y}$–$\hat{z}$ plane; that is, the phase function $P(\theta) \neq P(-\theta)$.

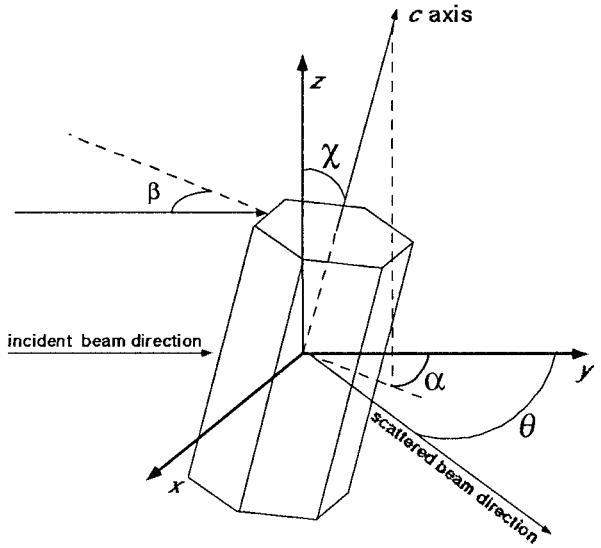

FIG. 2. Particle orientation and scattering angles. Orientation of the particle is described by the three Euler angles χ, α, and β, which, together with scattering angle θ, specify the scattering geometry. We define β to be the angle between the incident-beam direction and the projection of the a face normal onto the x–y plane.

3. Results: Vertical alignment ($\chi \sim 0°$)

a. General features

The main features we observed for this crystal orientation are classified as follows.

1) A ''halo'' peak in the range $22° < \theta < 35°$, usually the strongest feature for vertically aligned hexagonal particles.
2) A second peak in the $30° < \theta < 70°$ range, usually with weaker intensity than the halo peak but often modulated by coherent oscillations.
3) A backscatter peak in the $115° < \theta < 160°$ range with weaker intensity than the halo peak, sometimes modulated by oscillatory envelopes.

Figure 3 is a plot of the differential scattering cross section from a typical columnar ice crystal oriented vertically, illustrating the features described above. Here, 10 scans from a single scan series are overplotted to illustrate the typical degree of reproducibility between scans. We attribute the observed changes in peak amplitude (up to 50%) to small changes in crystal orientation between scans; this point will be discussed further in section 5b. However, the peak positions and peak widths remain fairly constant. The top- and side-view images are also shown here; note that the crystal orientation shown in the top view is the same as illustrated

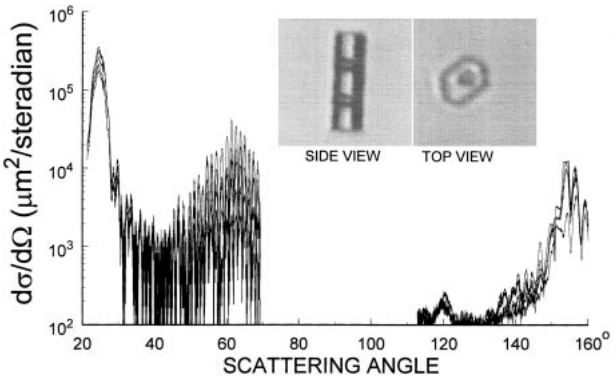

FIG. 3. Differential scattering cross section of a columnar ice crystal 79 μm long and 34 μm across. The 10 scans from groups 1 and 3 are overplotted, showing forward and backward scattering, respectively. The image (inset) was recorded 15 s prior to the first data scan; rotation of a few degrees occurred between groups 1 and 3.

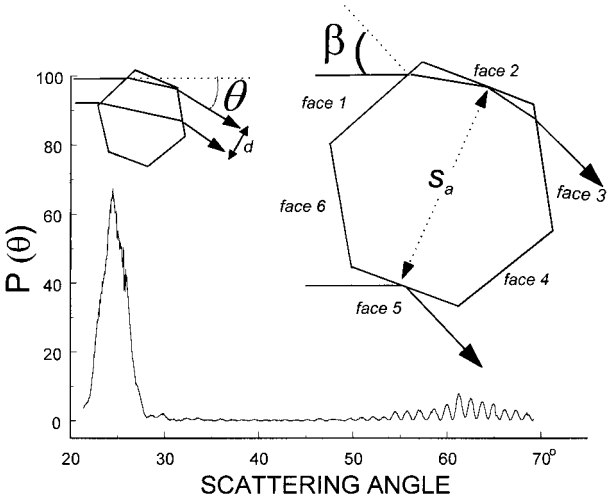

FIG. 4. Light-scattering phase function and the origin of forward-scattering features. A scan from Fig. 3 is plotted on a linear scale, with diagrams showing the rays responsible for the peaks. Also shown are *a* faces 1–6, face separation s_a, incident angle β, scattering angle θ, and ray family width *d*. The ripple feature near 60° comes from interference between two reflections, each of which undergoes a deviation $\theta_r = 2\beta - 60°$. Fourier analysis of the ripple structure provides a measurement of s_a (see Fig. 6).

in Fig. 1. Columnar crystals often developed hollowing on the basal faces, a feature that is often omitted from ice crystal scattering simulations but is known to be present in atmospheric ice particles. The crystal shown in Fig. 3 contained bubblelike imperfections; the effects of hollowing and defects will be discussed later.

In the following paragraphs we discuss the origin of features found for crystals oriented at various β values with $\chi \approx 0$.

b. Forward quadrant

1) ORIGIN AND LOCATION OF THE PEAKS

We identify two scattering features in the angular range 20°–65°, which we shall term ''halo peak'' and ''reflection peak'', although the latter often appears as a series of peaks or ripples. Figure 4 shows one of the scans from Fig. 3 converted to a phase function (see section 2b) and plotted on a linear scale. We have inset ray diagrams showing the rays responsible for the two features as well as definitions of θ, β, s_a, and faces 1–6. The halo peak we measure results from rays entering face 1 and leaving face 3, being refracted twice in the process: Snell's law predicts the deviation (scattering) angle θ_h to be

$$\theta_h = \beta - 60° + \arcsin\left\{ n \sin\left[60 - \arcsin\left(\frac{\sin\beta}{n} \right) \right] \right\}, \quad (2)$$

where n is the refractive index. For $n = 1.31$, the usual value for ice in the visible, Eq. (2) has a minimum at 21.8° (resulting in the well-known 22° halo observed when hexagonal crystals are randomly distributed in an optically thin cloud). In this case, β is 41.0° and the internal ray is parallel to face 2. Note that, for β between about 13.5° and 30°, there are two possible halo peaks as rays enter adjacent faces with incident angles β and $\beta + 60°$. For $\beta < 13.5°$, the ray is totally internally reflected at face 3 and there is no halo peak (although the adjacent *a* face will produce a halo peak for $\beta + 60°$). The internally reflected rays in this case produce a strong feature in the backscatter that we discuss in section 3c.

The second feature is more complex in origin. It results in part from a single external reflection at face 5, for which the deviation angle θ_r is given by

$$\theta_r = 2\beta - 60°, \quad (3)$$

where β is measured at face 1. For values of β greater than 41°, some of the rays entering face 1 are internally reflected at face 2 before exiting face 3. Because of the angular symmetry, the deviation of these rays is also given by Eq. (3); in effect, the two refractions cancel. Thus for most of the detection range $20° < \theta < 65°$, corresponding to $40° < \beta < 62.5°$, this reflection peak has two components. In the case of coherent monochromatic light, this results in the interference that we observe, which we shall discuss below. It is evident that the measured scattering exhibits continuous peaks of finite width, in contrast to the delta functions implied by ray tracing [Eqs. (2) and (3)]. In later sections we discuss the extent to which the peak widths can be attributed to finite-size effects (diffraction) and to crystal imperfections.

As an aside, we note that, for limited ranges of β, we expect that there are at least two other beams that emerge at the angle given by Eq. (3), involving multiple internal reflections: both enter face 1 and exit face 3, undergoing, respectively, internal reflections at faces 3, 5, and 1 and at faces 3, 5, 1, and 2. For a perfect hexagon, the former is possible for $41° < \beta < 53°$ and the latter for $55° <$

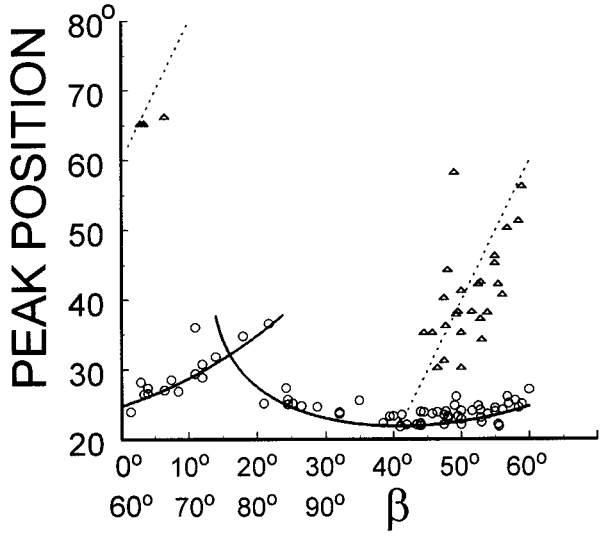

FIG. 5. Halo and reflection peak positions as functions of incident angle β. Measured positions of halo (open circles) and reflection (triangles) peaks are shown with the predictions of Eqs. (2) and (3) (solid and dashed lines, respectively). Because of the hexagonal symmetry, β is defined modulo 60°, and the model predictions are shown wrapped around 60°.

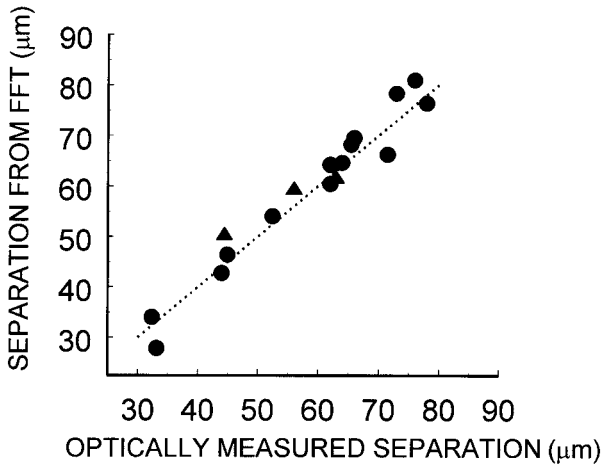

FIG. 6. FFT method for crystal size determination. Crystal face separations measured from ripple periodicity in the reflection peak [see Eq. (4)] are compared to optical measurements. Triangles are for basal faces separation, circles are for prism faces. The dotted line indicates 1:1 agreement.

$\beta < 63°$. We will not discuss these beams in detail; we estimate them to be orders of magnitude weaker than the more direct beams shown in Fig. 4.

The positions of the two scattering features in the data of Fig. 3 are consistent with the measured β of 51° and Eqs. (2) and (3), within experimental errors. In Fig. 5 we extend this comparison to all our scattering measurements with $\chi \sim 0°$. The data points shown are the measured halo and reflection peak locations (i.e., peak maxima) and the lines show the predictions of Eqs. (2) and (3). The data are consistent with the predictions to within the experimental errors in β and θ. These data validate our orientation measurements and are consistent with a crystal refractive index of 1.31.

2) Interpretation of the reflection peak

An understanding of the origin of the reflection peak allows us to deduce information on both crystal size and orientation from the measured scattering. The reflection peak position θ_r together with Eq. (3) can be used to infer β. (While the same is true for the halo peak position θ_h, interpretation is difficult because the halo peak location, given by Eq. (2), varies slowly with β, is not single valued, and depends on the refractive index n. A limitation of this method is that the reflection peak tends to be rather broad, typically 5° in width, leading to an error of about 2.5° in the inferred value of β.

For $\beta > 41°$, the reflection peak is the sum of two beams (see Fig. 4), each of which we assume is broadened by diffraction. The result is akin to Young's fringes, in which semicircular wavelets propagating from each slit reinforce at periodically selected angles (Born and Wolf 1959). To calculate the periodicity of the resulting ripples, we consider wavelets propagating from the right-hand edge of faces 2 and 5 (see the diagram in Fig. 4). The path difference between these beams is given by $\delta = s_a \cos(\theta/2 + \epsilon)$, where ϵ represents the beam spreading. Expanding for small angles ϵ, we find that the ripple separation ϵ_r is

$$\epsilon_r = \frac{\lambda}{s_a \cos(\theta_r/2)}. \tag{4}$$

Measurement of ripple separation ϵ_r and peak maximum θ_r allows the face separation s_a to be inferred. To test the idea quantitatively, we used a fast Fourier transform (FFT) technique to measure ϵ_r for reflection peaks exhibiting ripple structure, rejecting spectra that did not exhibit a clear single spectral peak. From this, we use Eq. (4) to deduce s_a, which we compare with s_a measured optically from the telemicroscopic crystal images. The results are shown in Fig. 6. The two datasets are 98% correlated, with an rms deviation of 6% (note that the optical measurements themselves carry an error of about 5%). We conclude that Eq. (4) does describe the ripple separation, and that it can be used to measure crystal dimensions.

3) Peak widths and amplitudes

One approach to calculating the far-field scattering pattern is to perform a Kirchoff integral over the exiting ray family (Born and Wolf 1959; Muinonen 1989). In the geometric limit, the incident beam can be broken up into ray families according to the projected area of the facets and by the appropriate transmissivity and reflectivity (Born and Wolf 1959, p. 341) at the crystal boundaries. Each ray family consists of a bundle of rays

that all follow the same refractions and reflections at crystal boundaries. Each feature in scattering can be attributed to one or more ray families (e.g., the reflection peak can be attributed to at least two ray families). For the case $\chi = 0°$, we use simple geometry to compute the width of the ray families responsible for the peaks we observe. From this, we can estimate the expected peak width, based on a single-slit analogy. The total peak cross section follows from the ray family width and the relevant transmission and reflection coefficients.

Essentially, rays leaving a crystal facet, due either to refraction or reflection, are analogous to those passing through single slits, for which the diffraction peak width varies inversely with slit width. For a single slit of width d the Fraunhofer intensity is given by $I(s) \sim \sin^2(s)/s^2$, where $s = 2\pi d \sin\psi/\lambda$; the diffraction angle ψ is usually small enough that $\sin\psi \approx \psi$. The full width at half maximum for the function $I(s)$ is 2.78, hence the angular width $\Delta\psi$ is

$$\Delta\psi = \frac{2.78\lambda}{2\pi d}. \quad (5)$$

We identify the slit width d to be the width of the ray family (see Fig. 4), which is a fraction (typically between 0.2 and 1) of the prism-face width a (depending on β and crystal asymmetry). For our crystals, $a \approx 30$ μm, so the typical halo peak width should be between about 0.5° and 3°. The reflection peak envelope is generally wider, since it is produced by a narrower family of rays, particularly when the deviation θ_r is small. Since the crystals have finite height h, the peaks also have a vertical width w_z (which we expect to vary inversely with h), but our setup did not allow us to measure it.

We compared the widths of the halo peaks with those deduced by applying Eq. (5) to the ray family width calculated from the measured length a_3 of face 3 and β. The measured peaks are generally wider than the predicted peaks, by a factor of about 2; for example, the calculated halo peak width for the crystal of Figs. 3 and 4 is 1.5°, while the measured width is about 3°. We considered the possibility of crystal rotation within each scan, but dismiss this because our (strobed) video reveals this to be minimal on the timescale of a scan (20 ms). Moreover, θ_h is generally a slowly varying function of β (see Fig. 6), and a significant crystal rotation is needed to sweep out 1° in scattering angle θ_h.

According to our simple model, the halo peak cross section is a maximum at $\beta = 41°$, when all the rays incident on face 1 contribute. For $\beta > 30°$, the external reflection from face 5 contributes, and for $\beta > 41°$ it is boosted by the internal reflection at face 2. As beta increases past 41°, the projected area of face 1 diminishes and a greater portion of the rays are reflected at face 2, so that the reflection peak grows at the expense of the halo peak. Crystal asymmetry also has an effect on the relative peak cross sections; for example, lengthening faces 2 and 5 increases the reflection peak and, for $\beta > 41°$, decreases the halo peak.

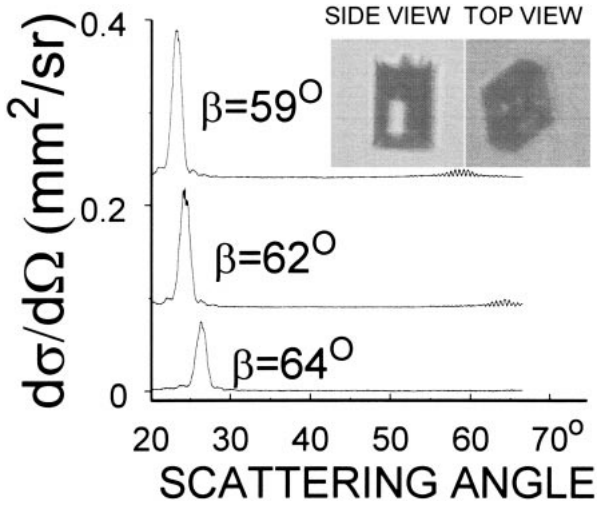

FIG. 7. Effect of crystal rotation during a scan series; scans from groups 1–3 are shown. For clarity, the differential scattering cross section has been shifted by the addition of constants. Note the peak movement and weakening of the halo peak as the particle (inset) rotates.

We observed the strongest halo peaks for β values near 41°, but we encountered a wide variability in peak strength between scan series for a given value of β, more than can be accounted for by crystal size or our measurement error of about 10%. We attribute this to the one-dimensional nature of the photodiode array; what we measure is only a section 0.5° wide through a peak in a two-dimensional scattering surface. If $\chi \neq 0$, the peak may not be centered on our array, leading to the variations that we observe.

Within a scan series, rotation of the crystals sometimes caused the peak to ''walk'' to the right and weaken. An example of this is shown in Fig. 7, in which an unusually large rotation took place over the three scan groups. We deduce β for each scan group from the location θ_r of the reflection peak (with distinctive ripple stucture) and Eq. (3). (In the final group we used the halo peak location.) As β increases, the peak cross section falls off, in qualitative agreement with predictions based on our simple model. For quantitative comparison of data and model, one must measure the total cross section for each peak by integrating over two-dimensional scattering data not yet available to us. However, by integrating over the measured peak in θ and assuming that the array samples the maximum of a Fraunhofer peak in the vertical direction, we are able to deduce a total cross section for each peak we measure. The assumption is questionable, even for cases with $\chi = 0$, and the cross sections deduced are quite variable and are at least 50% smaller than the model scattering cross sections.

c. Backscatter peaks

A subset of our scattering measurements were in the 115°–160° window. The peaks in this range were gen-

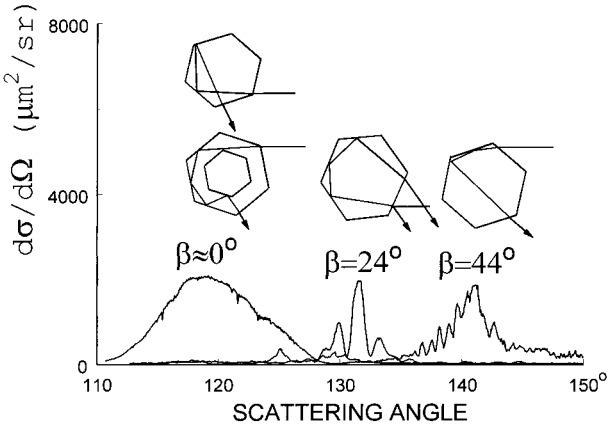

FIG. 8. Differential scattering cross section and origin of backscatter features from three different crystals. The features at 120° and 132° are from the column shown in Fig. 3 and the feature at 142° is from the plate shown in Fig. 10. The measured incident angle β is given for each, and suggested ray paths are drawn above the peaks.

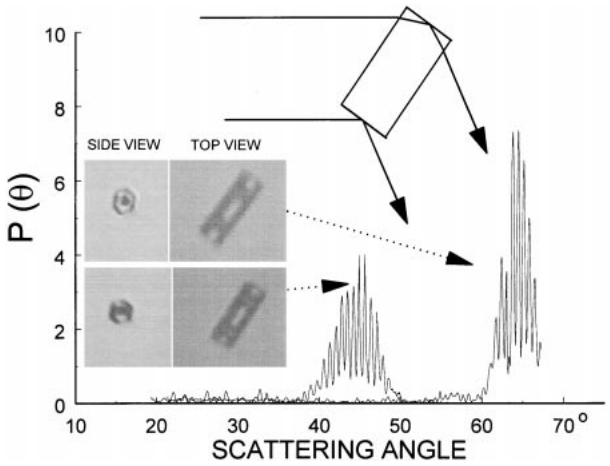

FIG. 9. Phase function and origin of reflection peaks for two horizontal orientations. An external reflection from one basal face interferes with an internal reflection from the other basal face. As with the prism faces, we can infer the basal face separation from the peak location and ripple periodicity (Fig. 6). Note how the peak moves as the particle rotates (the data shown are from two scan series 3 min apart).

erally broad and at least an order of magnitude weaker than the halo peak, as illustrated in Fig. 3. Figure 8 shows three features in this range (from different crystals), with diagrams showing possible ray paths for each. The angle β measured optically is shown for each feature. The feature at 132° is produced by both external and multiple internal reflections, with the deviation for both being given by $180° - 2\beta$ (here, β is the angle of incidence of laser 2 on the relevant prism face). The internal ray producing this feature is totally internally reflected for $\beta < 13.5°$, that is, when $\theta > 153°$, near the edge of our current detection range. As discussed by Takano and Jayaweera (1985), these multiple total internal reflections in hexagonal prisms contribute to a low asymmetry parameter g relative to circular cylinders. We attribute the modulation observed in the peak at 132° to interference between the internal and external reflections.

The feature at 142° is expected for $\beta > 41°$. It is relatively weak because the second internal reflection is only partial. The deviation for this ray path is calculated to be $120° + \theta_h(\beta)$, where θ_h is given by Eq. (2), such that the minimum deviation for this ray is 141.8°.

The feature at 120° has a stationary character (with respect to small variations in β) without interference modulation. We advance three ideas for its origin.

1) It may be an example of the 120° parhelion, in which internal reflections at faces 3 and 5 cause the ray to exit face 2 at precisely 120° (see, e.g., Greenler 1980).
2) It may be simply an external reflection with $\beta = 60°$.
3) It may be a result of the hollowing of columnar crystals.

An idea was put forward by Macke et al. (1996), who suggested that the thin shell of a hollowed crystal could act as a waveguide to scatter light at 120°. However, we could not reproduce the ray path offered by Macke et al. (1996) for a perfect hexagon and found that the scattering angle it implies is not quite 120°. We offer an alternative ray path for which $\theta = 120°$ independent of β over a range dependent on the shell thickness. One problem with this idea is that the internal shape may be rounded rather than hexagonal, a detail we were not able to discern from our images. If this were the case, then the peak may still appear, perhaps no longer centered at 120°.

Unfortunately, the top-view images for the hollowed crystal in which this feature was observed (in three separate scan series) were of poor quality, and we are unable at this point to distinguish between the three possibilities; both ray diagrams shown above this peak in Fig. 8 are consistent with the measurement error in this case. Nevertheless, its appearance did coincide with hollowing, and it may turn out to be a characteristic of hollowed columns. We hope to explore the scattering for $90° < \theta < 180°$ more fully in future experiments.

4. Results: Horizontal orientation ($\chi \approx 90°$)

Since ice crystals tended to orient vertically in our EDB, we studied only a few examples of horizontally oriented crystals. We did not observe the so-called 46° halo peak. However, for certain horizontal orientations we did observe reflection peaks that are directly analogous to those in the vertical orientation. In this case, glancing external and internal reflections from the basal faces undergo the same deviation and Eq. (4) also applies here, except we replace s_a with s_c, the separation between the basal faces. Figure 9 shows an example of

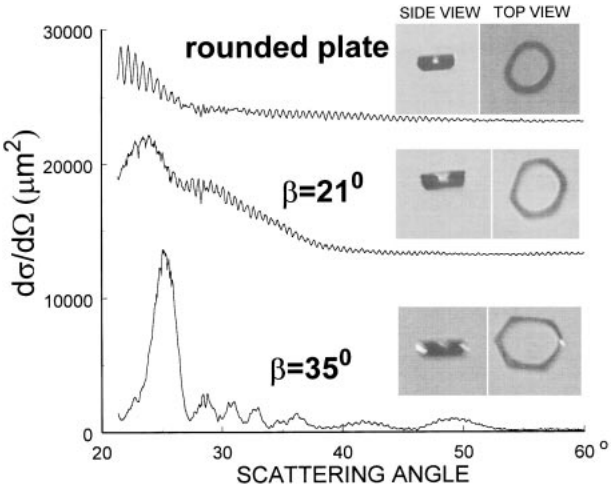

FIG. 10. Halo peak development as facets appear on an initially rounded plate crystal. Side and top views of the crystal (about 80 μm in diameter) are inset. For clarity, the data have been shifted by the addition of constants.

a reflection peak from the basal faces, with an effect analogous to two-beam interference. Note how the peak position changes with particle orientation; the peak location is consistent with a specular reflection from the basal face.

We repeated the FFT analysis described in section 3b(3) for the few cases in which the reflection peak was observed with a horizontal *c* axis, these data are shown in Fig. 6 as triangles. In this case, the relevant dimension is the separation of the basal faces s_c. We find that the method works well for cases in which the crystals were not hollowed. We often observe hollowing of the basal faces of columnar crystals with $s_c > 50$ μm, and in these cases the basal face is no longer faceted and there are no specular reflections.

5. Discussion and conclusions

a. Effects of surface roughness and imperfections

In Fig. 10 we show the evolution of scattering from a plate that was initially rounded. As the facets develop, the halo and reflection peak take the place of the undulations reminiscent of the scattering from a cylinder (Bohren and Huffman 1983). However, the side-view image reveals imperfections in the *a* faces (the facets are not fully formed), to which we attribute the width and low strength of the halo feature, and the persistence of the undulations.

Crystal imperfections on scales comparable with the wavelength of light will scatter light in all directions and irregularities such as surface roughness and hollowing are expected to modify $P(\theta)$. Modelers have now begun to include such effects but will require experimental (or field) data on which to base their parametrizations. In particular, surface roughness has been shown to have a profound effect on the modeled phase function, blurring or eliminating halo features (Hess et al. 1998; Yang and Liou 1998) and reducing the asymmetry parameter (Hess et al. 1998).

The forward and backscatter peaks we measure are generally wider than predicted by our simple single-slit model, which attributes the peak width solely to diffraction brought about by the narrowness of the ray family. If this crude model is sufficient, then our measured peak widths are consistent with a small degree of roughening, at most a few degrees of angular roughening [i.e., the variation of facet normal over the facet: what Hess et al. (1998) term ''tilt angle'']. The coherence of the interference structures such as those seen in Figs. 3, 7, and 9 suggests that the reflecting facets are often flat to within a wavelength (0.633 μm). Despite visible imperfections in the crystals, the intensity away from the peaks is, in the case of fully faceted crystals with size parameters $x > 200$, less than 1% of the halo peak intensity, indicating that the level of isotropic scattering was low. The case shown in Fig. 10 shows significant scattering away from the halo peak that is related to both rounded and imperfect facets. Surprisingly, hollowed crystals were not observed to scatter significantly away from the known peaks; for example, the scattering shown in Fig. 8 came from a crystal that was about 20% hollowed.

b. Effect of tilt ($\chi > 0°$) on peak amplitudes

We have restricted our analysis to crystals whose *c* axis was either nearly vertical or nearly horizontal. However, although small deviations (such as $\chi < 5°$) affect the total cross section of each peak only slightly, they can have a large effect on the peak amplitude measured with our linear array.

As an example of the effect of tilt, consider a crystal oriented with $\alpha = 90°$ and $\chi = 5°$ (i.e., tilted such that $\hat{c}$ remains perpendicular to the incident beam direction $\hat{y}$). By symmetry, the rays responsible for the peaks (halo and reflection) simply rotate with the crystal and are contained in a plane perpendicular to the *c* axis. The angle each ray makes with the horizontal plane (the vertical deviation) is given by $\arcsin(\sin\theta \sin\chi)$ − about 2° for the halo peak and 4° for the reflection peak. The case $\alpha = 0°$ is a little more complicated, but the effect is similar. We expect that the halo peak is shifted only slightly from the horizontal and that the two component reflection rays receive different vertical deviations because of the effect of refraction on the internally reflected ray. Since, in our measurement range, these are glancing reflections, the vertical deviation is greater for $\alpha = 90°$ than for $\alpha = 0°$.

Since the peak maxima of tilted crystals are not contained in the scattering plane, small differences in tilt can lead to large differences in measured amplitude; the severity of the effect depends on the vertical width of the peaks. It is likely that the variability in peak amplitude in our data is attributable in large part to small

changes in χ. Also, since the vertical deviation depends on scattering angle θ, amplitudes of peaks narrow in the vertical dimension that are measured at different θ with a linear array can be unreliable when $\chi \neq 0°$.

c. Comparison with models

Despite the large numbers of model studies on scattering by hexagonal particles, there are almost no published phase functions for fixed orientations; modelers prefer to average over all orientations. Ultimately, we would like to test more rigorous models such as the GOM2 model (Yang and Liou 1997); a preliminary test (P. Yang and K. N. Liou 1998, personal communication) reproduced general features, but the resolution in θ was not sufficient to demonstrate whether or not the ripple structure could be accurately modeled, and more extensive comparisons are needed to test peak positions, widths, and relative heights. In addition, we looked at two other studies that show results from fixed orientations: Rother et al. (1997) published model phase functions for infinite hexagonal prisms based on a discretized Mie formalism, for particular orientations. The size parameters in this study, based on cross-sectional diameter, were restricted to $x \leq 100$. However, the results show, for $x = 100$ and $\beta = 60$, a broad halo peak and hints of a reflection peak with ripple structure, features that also appear in our data. Barkey et al. (1999), in an analog experiment, report halo and reflection peak positions similar to those we observe (note that their definition of β differs from ours by 30°).

d. Conclusions

We present here the first measurements of light scattering from single ice particles with well-known shapes and orientations. The location of halo and reflection peaks in the $20° < \theta < 65°$ range agree with geometrical ray-tracing predictions to within experimental precision. Conversely, the reflection peak location θ_r can be used to deduce β independent of optical measurements. We have shown that the ripple structure, together with the peak location, can be used to measure the separation of both prism and basal faces. Also, peak locations in the range $115° < \theta < 160°$ are consistent with proposed ray paths.

Despite the relatively large parameter size of our particles ($x > 200$), we find that it is important to incorporate interference effects into the scattering model to account for the observed ripple structure in certain scattering features. Thus conventional ray-tracing schemes are not adequate to describe the scattering from single-oriented particles. It remains to be seen whether the differences are important for an ensemble of orientations and whether more sophisticated schemes such as GOM2 (Yang and Liou 1997) can reproduce all the observed single-particle features. The observed width of halo peaks from our fully faceted crystals may be consistent with a small degree of facet roughness, but we must first validate a model for the peak width of hexagonal crystals with flat facets. In general, the measured peak amplitudes (differential scattering cross section maxima) are less than predicted by our simple model, and we look forward to further measurements with a 2D detector to elucidate the effect of crystal tilt. Also planned are experiments with an extended range in the forward and backscattering direction (closer to 0° and 180°) using a recently completed chamber with improved optical access and an extended low-temperature range.

Acknowledgments. Support for this work came from the Leonard X. Bosack and Bette M. Kruger Charitable Foundation and NSF Grants ATM-9417445 and ATM-9528049. We wish to thank M. B. Baker and E. J. Davis for many valuable comments and guidance and T. C. Grenfell and S. G. Warren for comments on the manuscript. We wish to thank P. Yang and K. N. Liou of UCLA for some early comparisons with models and D. S. Covert for providing some instrumentation used during the startup of these experiments.

REFERENCES

Bacon, N. J., B. D. Swanson, M. B. Baker, and E. J. Davis, 1998a: Breakup of levitated frost particles. *J. Geophys. Res.,* **103,** 13 763–13 775.

——, ——, ——, and ——, 1998b: Laboratory measurements of light scattering by single ice particles. *J. Aerosol Sci.,* **29** (Suppl. 1), S1317–S1318.

Barkey, B., K. N. Liou, and Y. Takano, 1999: An analog light scattering experiment of hexagonal icelike particles. Part II: Experimental and theoretical results. *J. Atmos. Sci.,* **56,** 613–625.

Bohren, C. F., and D. R. Huffman, 1983: *Absorption and Scattering of Light by Small Particles.* Wiley, 530 pp.

Born, M., and E. Wolf, 1959: *Principles of Optics.* Pergamon, 803 pp.

Cai, Q., and K. N. Liou, 1982: Polarized light scattering by hexagonal ice crystals: Theory. *Appl. Opt.,* **21,** 3569–3580.

Draine, B. T., and P. J. Flatau, 1994: Discrete-dipole approximation for calculations. *J. Opt. Soc. Amer. A,* **11,** 1491–1499.

Dugin, V., and S. Mirumyantz, 1976: The light-scattering matrices of artificial crystalline clouds. *Izv. Atmos. Oceanic Phys.,* **12,** 988–991.

——, B. M. Golubitskiy, S. O. Mirumyants, P. I. Paramonov, and M. V. Tantashev, 1971: Optical properties of artificial ice clouds. *Izv. Atmos. Oceanic Phys.,* **7,** 871–877.

Francis, P. N., 1995: Some aircraft observations of the scattering properties of ice crystals. *J. Atmos. Sci.,* **52,** 1142–1154.

Greenler, R., 1980: *Rainbow, Halos, and Glories.* Cambridge University Press, 195 pp.

Gustafson, B. A. S., 1996: Microwave analog to light-scattering measurements: A modern implementation of a proven method to achieve precise control. *J. Quant. Spectrosc. Radiat. Transfer,* **55,** 663–672.

Hess, M., R. B. A. Koelemeijer, and P. Stammes, 1998: Scattering matrices of imperfect hexagonal ice crystals. *J. Quant. Spectrosc. Radiat. Transfer,* **60,** 301–308.

Heymsfield, A. J., and R. G. Knollenberg, 1972: Properties of cirrus generating cells. *J. Atmos. Sci.,* **29,** 1358–1366.

Kinne, S., T. Ackerman, A. Heymsfield, F. Valero, K. Sassen, and J. Spinhirne, 1992: Cirrus microphysics and radiative transfer:

Cloud field study on 28 October 1986. *Mon. Wea. Rev.,* **120,** 661–684.

Lawson, R. P., A. J. Heymsfield, S. M. Aulenbach, and T. L. Jensen, 1998: Shapes, sizes and light scattering properties of ice crystals in cirrus and a persistent contrail during SUCCESS. *Geophys. Res. Lett.,* **25,** 1331–1334.

Macke, A., 1993: Scattering of light by polyhedral ice crystals. *Appl. Opt.,* **32,** 2780–2788.

——, J. Mueller, and E. Raschke, 1996: Single scattering properties of atmospheric ice crystals. *J. Atmos. Sci.,* **53,** 2813–2825.

Mishchenko, M. I., L. D. Travis, and D. W. Mackowski, 1996: T-matrix computations of light scattering by nonspherical particles: A review. *J. Quant. Spectrosc. Radiat. Transfer,* **55,** 535–575.

Muinonen, K., 1989: Scattering of light by crystals: A modified Kirchoff approximation. *J. Appl. Opt.,* **28,** 3044–3050.

Pluchino, A., 1986: Observations of halo scattering from single ice crystals. *Opt. Lett.,* **11,** 276–278.

——, 1987: Scattering photometer for measuring single ice crystals and evaporation and condensation rates of liquid droplets. *J. Opt. Soc. Amer. A,* **4,** 614–620.

Rimmer, J. S., and C. P. R. Saunders, 1997: Radiative scattering by artificially produced clouds of hexagonal plate ice crystals. *Atmos. Res.,* **45,** 153–164.

Rother, T., K. Schmidt, and J. Wauer, 1997: Plane wave scattering on hexagonal cylinders. *J. Quant. Spectrosc. Radiat. Transfer,* **57,** 669–681.

Sasaki, Y., N. Nishiyama, and Y. Furukawa, 1998: Experimental study on light scattering from an artificial ice cloud. *Polar Meteor. Glaciol.,* **12,** 130–139.

Sassen, K., and K. N. Liou, 1979: Scattering of polarized laser light by water droplet, mixed-phase, and ice crystal clouds. Part I: Angular scattering patterns. *J. Atmos. Sci.,* **36,** 838–861.

Stackhouse, P. W., Jr., and G. L Stephens, 1991: A theoretical and observational study of the radiative properties of cirrus: Results from FIRE 1986. *J. Atmos. Sci.,* **48,** 2044–2059.

Stephens, G. L., S. C. Tsay, P. W. Stackhouse, and P. J. Flatau, 1990: The relevance of the microphysical and radiative properties of cirrus clouds to climate and climate feedback. *J. Atmos Sci.,* **47,** 1742–1753.

Swanson, B. D., N. J. Bacon, E. J. Davis, and M. B. Baker, 1999: Electrodynamic trapping and manipulation of ice crystals. *Quart. J. Roy. Meteor. Soc.,* **125,** 1039–1058.

Taflove, A., 1995: *Computational Electrodynamics: The Finite-Difference Time Domain Method.* Artech House, 599 pp.

Takano, Y., and K. Jayaweera, 1985: Scattering phase matrix for hexagonal ice crystals computed from ray optics. *Appl. Opt.,* **24,** 3254–3263.

——, and K. N. Liou, 1989: Solar radiative transfer in cirrus clouds. Part I: Single-scattering and optical properties of hexagonal ice crystals. *J. Atmos. Sci.,* **46,** 3–19.

——, and ——, 1995: Radiative transfer in cirrus clouds. Part III: Light scattering by irregular ice crystals. *J. Atmos. Sci.,* **52,** 818–837.

Vogelmann, A. M., and T. P. Ackerman, 1995: Relating cirrus cloud properties to observed fluxes: A critical assessment. *J. Atmos. Sci.,* **52,** 4285–4301.

Volkovitskiy, O. A., L. N. Pavlova, and A. G. Petruskin, 1980: Scattering of light by ice crystals. *Izv. Atmos. Oceanic Phys.,* **16,** 98–102.

Yang, P., and K. N. Liou, 1995: Light scattering by hexagonal ice crystals: Comparison of finite-difference time domain and geometric optics models. *J. Opt. Soc. Amer. A,* **12,** 162–176.

——, and ——, 1996: Finite-difference time domain method for light scattering by small ice crystals in three-dimensional space. *J. Opt. Soc. Amer. A,* **13,** 2072–2085.

——, and ——, 1997: Light scattering by hexagonal ice crystals: Solutions by a ray-by-ray integration algorithm. *J. Opt. Soc. Amer. A,* **14,** 2278–2289.

——, and ——, 1998: Single-scattering properties of complex ice crystals in terrestrial atmosphere. *Contrib. Atmos. Phys.,* **71,** 223–248.